Taylor & Francis
Taylor & Francis Group

Journal of Asian Architecture and Building Engineering

ISSN: (Print) (Online) Journal homepage: https://www.tandfonline.com/loi/tabe20

Shear strength and cracking behavior of reinforced concrete nonstructural walls

Miki Matsubayashi, Yuya Takase & Mitsuo Mizoguchi

To cite this article: Miki Matsubayashi, Yuya Takase & Mitsuo Mizoguchi (2020): Shear strength and cracking behavior of reinforced concrete nonstructural walls, Journal of Asian Architecture and Building Engineering, DOI: 10.1080/13467581.2020.1838290

To link to this article: https://doi.org/10.1080/13467581.2020.1838290

Published online: 03 Nov 2020.

JOURNAL OF ASIAN ARCHITECTURE AND BUILDING ENGINEERING
https://doi.org/10.1080/13467581.2020.1838290

Taylor & Francis
Taylor & Francis Group

BUILDING STRUCTURES AND MATERIALS

Shear strength and cracking behavior of reinforced concrete nonstructural walls

Miki Matsubayashi[a], Yuya Takase[b] and Mitsuo Mizoguchi[b]

[a]Division of Sustainable and Environmental Engineering, Muroran Institute of Technology, Muroran, Japan; [b]College of Design and Manufacturing Technology, Muroran Institute of Technology, Muroran, Japan

ABSTRACT

Recent Japanese earthquakes have severely damaged the nonstructural walls of many buildings. While nonstructural walls do not influence the seismic performance of a building, this damage can still sometimes cause buildings to be demolished or render their continued use impossible. Therefore, it is important that seismic designs take the seismic properties of nonstructural walls into consideration. Shear loading tests and FE analysis were conducted to investigate this phenomenon, which showed that shear strength decreased and crack width increased with wider rebar spacing. The FE analysis indicated that the discrete crack model evaluated the test results more adequately than the smeared crack model. In addition, the stress distribution was localized with wider rebar spacing. Therefore, it is thought that the shear strength decreased. Finally, a simple crack width prediction method was proposed. With this method, the rebar strain was calculated using the horizontal deformation of the walls. Using this method, the crack width could be reasonably estimated. It is believed that these findings will be useful for designing nonstructural walls with improved seismic performance.

ARTICLE HISTORY
Received 29 May 2020
Accepted 14 October 2020

KEYWORDS
Nonstructural wall; damage quantity; crack width prediction; discrete crack model

1. Introduction

Japan has experienced many major earthquakes and has suffered from the resulting damage to large buildings for a long time. The seismic design of buildings has evolved through investigating this building damage. The current Japanese seismic design code was established in 1981. After the Kobe Earthquake, which occurred in 1995, few of the buildings that had collapsed or sustained severe structural damage were designed after 1981. However, nonstructural members have continued to sustain severe damage during recent large earthquakes.

In reinforced concrete (RC) buildings, a structural design is not required for nonstructural walls, e.g., mullion walls, while spandrel walls beside a column need to be structurally designed. Therefore, even if such nonstructural walls, which need not be structurally designed, were severely damaged during an earthquake, there would be no danger to the building. However, there have been several reports of severe damage to nonstructural walls following major earthquakes in recent years. Figure 1 shows an example of a nonstructural wall damaged during the 2016 Kumamoto earthquake. Although damaged nonstructural walls do not affect structural safety, they sometimes cause other problems. For example, some buildings were demolished because rapid recovery was impossible due to high repair costs. Therefore, it is vital to address the problems caused by damage to nonstructural members to allow the continued use of a building after a large earthquake.

Previous studies on damages of nonstructural walls mainly focused on the brick wall (Maidiawati, Sanada, Konishi, and Tanjung 2011), the influence of a nonstructural wall on the collapse of an RC frame (e.g. Tsai and Huang 2011), the economic losses and cost benefits of retrofitting (Sousa and Monteiro 2018) and others. More recently, the number of researches for RC nonstructural walls have been increasing, especially after the 2011 Tohoku earthquake and tsunami. The earthquake damaged many nonstructural walls. Takase, Ikeda, and Suzumura (2015) reported that the nonstructural walls were severely damaged in the earlier stages of the earthquake motion, although the duration of motion of the 2011 Tohoku earthquake and tsunami was sufficiently longer for approximately five minutes in the Tohoku region. After the 2016 Kumamoto earthquake, a building with RC nonstructural walls was analyzed, subsequently, the effect of nonstructural walls on the seismic performance of the building was also investigated (Suzuki, Sanada, and Choi 2017).

Sanada et al. (2017) revealed that the softening of nonstructural flat walls decreased the building ductility. Yoon et al. (2017) pointed that nonstructural walls increased the stiffness and strength of the RC frames. Fukui, Sanada, and Yoon (2019) analyzed the same to evaluate an axial compression which applied to a nonstructural flat wall. On the other hand, retrofitting methods for nonstructural RC walls were also investigated (Tani et al. 2015).

CONTACT Yuya Takase y.takase@mmm.muroran-it.ac.jp , Muroran, Hokkaido 050-8585, Japan

Figure 1. Example of a damaged non-structural wall.

Although various researches on RC nonstructural walls have been conducted, it is observed that findings on its seismic properties, which include shear strength, cracking patterns, etc., are still limited.

The purpose of this study is to determine the relationship between the shear capacity of RC nonstructural walls and quantity of damage sustained. In this research, mullion walls were used as nonstructural walls. The Japanese guidelines (AIJ 2010) mainly require the following specifications for structural walls: i) a rebar ratio p_w of more than 0.25 %, and ii) a wall thickness t of 120 mm or more. In this study, firstly, shear loading tests are conducted. Eight full-size wall specimens are prepared with wall thicknesses of 100 mm, making them all nonstructural walls according to the Japanese guidelines. The test parameters are the rebar spacing and the rebar ratio. Additionally, a finite-element (FE) analysis is conducted to investigate the relationship between the stress field and the rebar arrangement. Finally, a crack width prediction method is proposed. From these investigations, the shear capacity and damage quantity are comprehensively evaluated.

2. Test plan and result

2.1. Details of specimens

Eight specimens were manufactured. These specimens are modeled as walls with neighbor openings, as shown in Figure 1. Table 1 lists the test parameters, while Tables 2 and 3 show the material properties of the concrete and the rebar, respectively. All the deformed bars are regulated by the Japanese Industrial Standard (JIS G3112). For concrete, normal Portland cement is used, and the maximum aggregate size is 20 mm.

The specimens are divided into two series: Series A and Series B. The specimens are named S110, S220, S280, and M200 for Series A, and SS180, M320, M50, and L130 for Series B. The first letter of each name indicates the index of the rebar ratio p_w in the increasing order of SS, S, M, and L. The following number indicates the rebar spacing. Figure 2 shows the shapes of Series A and Series B specimens. The specimens of Series A have 100 mm x 750 mm cross sections and 750 mm heights, while the specimens of Series B have 100 mm x 700 mm cross sections and 700 mm heights. Figure 3 shows the rebar arrangement of all specimens.

For S110, S220, and S280 of Series A, the main test parameter is the rebar spacing. S220 is a medium specimen. In S220, ϕ6 rebar (with a spacing of 220 mm) and ϕ16 rebar are applied to the wall and the opening reinforcement, respectively. The opening reinforcement bars are common among all specimens. These rebar ratios are in the range of 0.26–0.29 %. While p_w is larger than 0.25%, which is applied to a structural wall in the Japanese guidelines, these ratios are sufficiently small compared to the actual shear wall. Although M200 has roughly the same rebar spacing as S220, the rebar ratio is approximately twice that of S110 to S280. The specimens have a loading beam and a bottom beam, which are 1550 mm x 260 mm x 470 mm and 1550 mm x 260 mm x 400 mm, respectively. Eight ϕ19 bars are used for a longitudinal bar, and ϕ10 bars are used for a transversal bar with 150 mm spacing.

For Series B, SS180 has a p_w of 0.18 %, which is the smallest in this test, while L130 has the highest p_w. M320 and M50 have the largest and smallest spacings, respectively. Similar to Series A, Series B specimens have loading beams and bottom beams, which measure 1500 mm x 600 mm x 300 mm and 1500 mm x 600 mm x 300 mm, respectively. Once again, eight ϕ19 bars are used for a longitudinal bar, and ϕ10 bars are used for a transversal bar with 150 mm spacing.

Table 1. Parameter of specimens.

Series	A	A	A	A	B	B	B	B
Specimens	S110	S220	S280	M200	SS180	M320	M50	L130
Wall thickness (mm)	100	100	100	100	100	100	100	100
Wall length (mm)	750	750	750	750	700	700	700	700
Wall height (mm)	750	750	750	750	700	700	700	700
Wall rebar	ϕ6	2- ϕ 6	ϕ10	2- ϕ6,10	ϕ6	ϕ16	ϕ6	ϕ13
Rebar spacing (mm)	110	220	280	200	180	320	50	130
Rebar ratio (%)	0.29	0.29	0.25	0.52	0.18	0.62	0.63	0.97
Opening rebar	ϕ16	ϕ16	ϕ16	ϕ16	ϕ16	ϕ19	ϕ19	ϕ19
Shear span ratio	0.5	0.5	0.5	0.5	0.5	0.5	0.5	0.5
Cover thickness (mm)	36	30	40	30	30	30	30	30
Axial load (kN)	308	303	291	300	283	263	272	276
Axial load ratio	0.15	0.15	0.15	0.15	0.15	0.15	0.15	0.15

Table 2. Material properties of concrete.

Specimens	S110	S220	S280	M200	SS180	M320	M50	L130
f_c	27.5	27.0	25.9	26.8	26.3	25.9	25.1	27.0
E_c	25.8	25.7	25.3	25.6	21.1	20.5	20.2	20.4
f_t	2.15	2.17	2.01	1.96	1.81	1.83	1.58	1.79

f_c: Compressive strength (N/mm^2), E_c: Young`s modulus (kN/mm^2), f_t: Split strength (N/mm^2)

Table 3. Material properties of rebar.

Rebar diameter	ϕ6	ϕ6	ϕ10	ϕ13	ϕ16	ϕ16	ϕ19
Series	A	B	A	B	A	B	B
f_y	439	375	400	398	387	395	401
E_s	184	177	172	179	175	173	180
f_u	571	538	547	513	567	534	560
Δ	-	13.7	-	16.8	-	14.9	14.5

f_y: Yield strength (N/mm^2), E_S: Young`s modulus (kN/mm^2), f_u: Ultimate strength (N/mm^2), Δ: Elongation at rupture (%)
* Elongations of Sirise A were not measured because of an error.

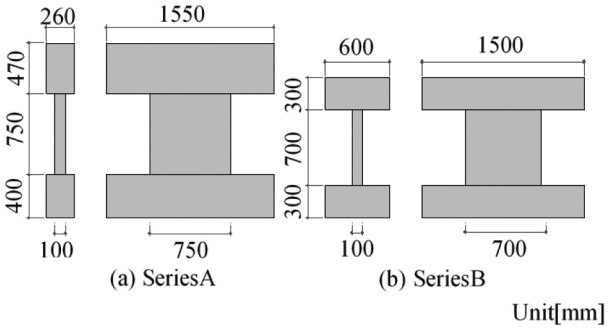

Figure 2. Shapes of specimens.

2.2. Loading method

In this test, reversed cyclic shear loading is applied to the specimens. A constant axial load is also applied. The axial stress ratio, which is the ratio of the axial stress to the concrete compressive strength, is 0.15. In a structural design, it is not imperative for nonstructural walls to bear axial forces. However, according to the previous paper (Fukui, Sanada, and Yoon 2019), it was observed that an axial stress ratio of approximately 0.4 could be attained in nonstructural walls via analytical investigation. Furthermore, it is possible for the specimens to fail in flexure, when the axial stress ratio is zero, while mullion walls failed in shear during the earthquakes, as shown in Figure 1. Therefore, in these tests, the axial stress ratio is determined so as to prevent a flexure failure. To achieve this, the axial stress ratio was set to 0.15, which was also used in previous tests (e.g., Tani et al. 2015).

The shear load is controlled by the drift angle R, which is the value of the horizontal displacement of the loading beam δ divided by the wall height h.

Figure 4 shows the loading setup, while Figure 5 shows the image of the flow of automatic control and the data measurement methods. A shear load is applied such that the loading beam is parallel and an antisymmetric moment is created. To maintain the parallel state, two actuators are used in the vertical direction. The axial load is applied by an actuator positioned at the center of the wall. The control procedure is as follows: i) the vertical displacements of the two points of the beam are measured in order to confirm that the beams are parallel, ii) an AD converter is used to convert the measured value into a digital signal, iii) a control program (LabVIEW software) is used to calculate the output voltage such that the loading beam and bottom beam become parallel, and iv) the output voltage is converted into an analog signal to control the actuator.

In the horizontal direction, a reversed cyclic load is applied by the actuator installed at the center height

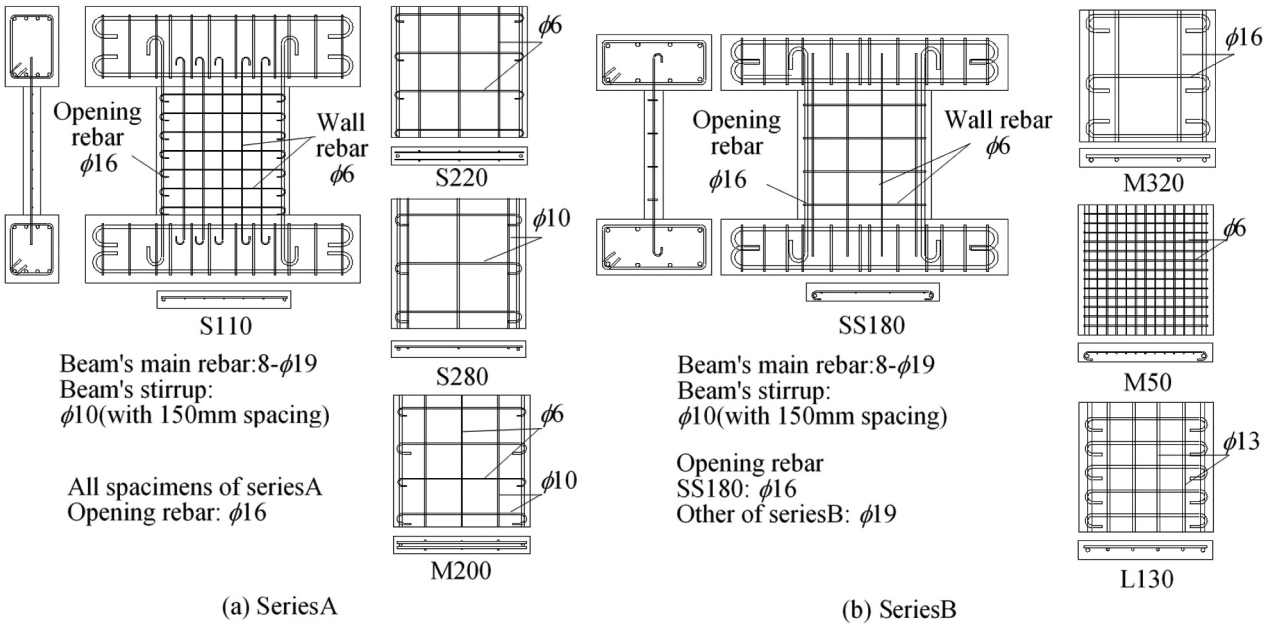

Figure 3. Rebar arrangement.

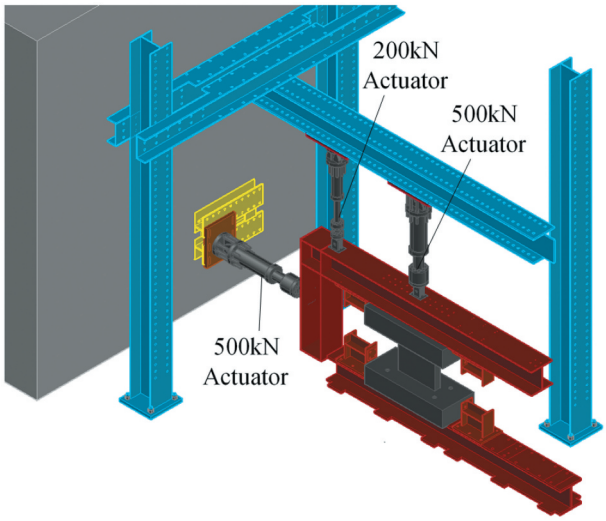

Figure 4. Loading setup.

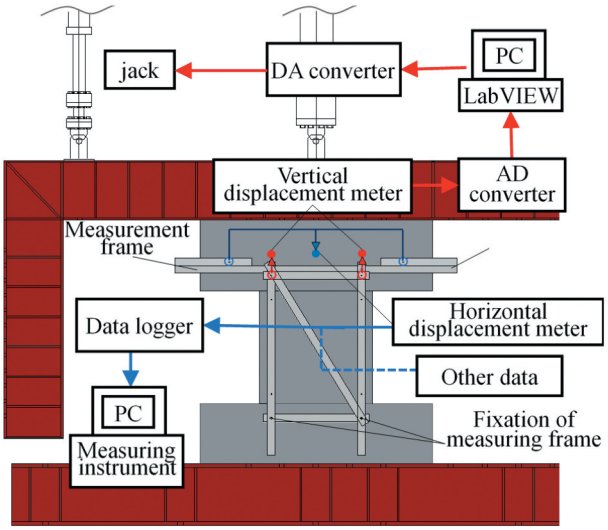

Figure 5. Image of flow of measurement and controlling.

position of the wall. The horizontal load is gradually increased in the following increments: $R = 0.1 \times 10^{-2}$, 0.2×10^{-2}, 0.3×10^{-2}, 0.4×10^{-2}, 0.5×10^{-2}, 0.6×10^{-2}, and 0.8×10^{-2} rad.

2.3. Crack width measurement method

A crack scale is used to measure the crack width ω. The resolution is 0.05 mm in ω = 0.05 ~ 1 mm, 0.1 mm in 1 ~ 1.4 mm, and 1 mm after 1.4 mm. The maximum crack width of each loading step is measured after the shear load is decreased by approximately 10% from the peak displacement of that step. In addition, the residual crack widths are measured when the shear load is 0 kN while changing from unloading to reloading. Cracks and exfoliations that could be visually confirmed are recorded by a sketch. The crack width is measured on both surfaces of the wall.

2.4. Test results

2.4.1. Maximum load and load – deformation relationship

Table 4 shows the maximum load Q_{max}, maximum shear stress τ_{max}, and deformation angle at the maximum load R_{max}. The maximum shear stress is the value of the maximum load divided by the wall cross section. Table 5 compares the test results with the calculated shear strength. In this paper, the following formulas are used from the Japanese guidelines (AIJ 2010).

$$ {}_{su}Q_{mean} = \left\{ \frac{0.068 p_t^{0.23}(18+f_c)}{\sqrt{\frac{M}{Qd}+0.12}} + 0.85\sqrt{p_{se} f_{wy}} + 0.1\sigma_0 \right\} b \cdot j \quad (1a) $$

$$ {}_{su}Q_{min} = \left\{ \frac{0.053 p_t^{0.23}(18+f_c)}{\sqrt{\frac{M}{Qd}+0.12}} + 0.85\sqrt{p_{se} f_{wy}} + 0.1\sigma_0 \right\} b \cdot j \quad (1b) $$

$$ {}_{mu}Q = \left\{ f_y a_t l_t + 0.5 f_{wy} a_{se} l_w + 0.5 N l_w \right\} / h_w \quad (2) $$

Equation (1a) is used to estimate the mean shear strength, while Equation (1b) is applied when a lower limit strength is calculated. ${}_{mu}Q$ is the shear force at ultimate flexural moment. In previous guidelines, there seemed to be no standards for an ultimate flexural moment of a nonstructural flat wall without columns. Therefore, Equation (2) is configured by using some previous guidelines (e.g., JBDP 2017) as a reference.

Table 4 lists τ_{max} values for S110, S220, and S280 and shows that τ_{max} decreases as the rebar spacing increases. Compared with S220, τ_{max} is 12% higher for S110. A similar tendency is confirmed in the τ_{max} values for M50 and M320. The results of S220 and M200 also confirm that τ_{max} decreases when the rebar ratio decreases. Although the rebar spacing is slightly different, a similar trend is observed in the results of S110 and L130.

Focusing on Table 5, $Q_{max}/{}_{su}Q_{mean}$ ranges from 0.82 to 1.15. When ${}_{su}Q_{min}$ is applied, the calculated value exceeds the test value except for M320. For M320, although the p_w value of 0.62 % is large enough to allow it to be applied to an actual shear wall, the spacing is wider. In the Japanese guidelines, the rebar spacing of a shear wall must be smaller than 300 mm. Therefore, when the rebar spacing is wider, Equation (1b) cannot be used to calculate a lower limit strength.

Figure 6(a-h) show the load–deformation curves. In all the figures, the maximum loads are marked. For S110 in Figure 6(a), the shear load peaked when $R = 0.23 \times 10^{-2}$ rad. After the peak load, the cracks expanded rapidly, and at $R = 0.50 \times 10^{-2}$ rad, the deformation increased drastically. For all other specimens except S220, the load also peaked at R ≅ 0.2rad, and the specimens failed at

Table 4. Test results.

Specimens	S110	S220	S280	M200	SS180	M320	M50	L130
Q_{max} (kN)	305.0	272.4	259.6	301.3	214.2	230.7	280.8	291.2
τ_{max} (N/mm^2)	4.06	3.63	3.46	4.02	3.06	3.30	4.01	4.16
R_{max} (*10^{-2} rad)	0.23	0.20	0.21	0.40	0.22	0.30	0.49	0.51

Table 5. Comparison of test results with calculated shear strength.

Series	A	A	A	A	B	B	B	B
Specimens	S110	S220	S280	M200	SS180	M320	M50	L130
p_t (%)	0.26	0.26	0.26	0.26	0.28	0.41	0.41	0.41
F_c (N/mm^2)	27.5	27.0	25.9	26.8	26.3	25.9	25.1	27.0
M/Qd	0.5	0.5	0.5	0.5	0.5	0.5	0.5	0.5
p_{se} (%)	0.29	0.29	0.25	0.52	0.18	0.62	0.63	0.97
f_{wy} (N/mm^2)	439	439	400	439	375	395	375	398
b (mm)	100	100	100	100	100	100	100	100
j (mm)	623.4	623.4	623.4	623.4	581.9	581.9	581.9	581.9
Q_{max} (kN)	305.0	272.4	259.6	301.3	214.2	230.7	280.0	291.2
$_{mu}Q$ (kN)	427.6	401.3	433.5	488.0	387.5	507.1	499.6	550.4
$_{su}Q_{mean}$ (kN)	265.0	262.5	251.1	281.7	229.2	279.8	274.6	305.2
$_{su}Q_{mean}/_{mu}Q$	0.62	0.65	0.58	0.58	0.59	0.55	0.55	0.55
$Q_{max}/_{su}Q_{mean}$	1.15	1.04	1.03	1.07	0.93	0.82	1.02	0.95
$_{su}Q_{min}$ (kN)	225.3	223.3	212.8	242.6	192.6	240.1	235.7	264.6
$Q_{max}/_{su}Q_{min}$	1.35	1.22	1.22	1.24	1.11	0.96	1.19	1.10

R ≅ 0.5rad. These results indicate that these specimens failed by a diagonal tension failure mode.

On the other hand, for S220, rapid deformation after a peak was not observed because this was the only specimen to experience failure in a compressive strut. SS180 had the lowest maximum shear stress among all specimens. SS180 did not experience any damage on the negative side even before the peak load in positive. Therefore, the negative shear load was applied afterward, and the shear failure also occurred on the negative side.

2.4.2. Crack pattern

Figure 7 shows the crack patterns when $R = 0.3 \times 10^{-2}$ rad, as well as the ultimate deformation. Black and red lines in the figures indicate cracks generated on the positive and negative sides, respectively. In the figures for Series A, the four white circles illustrated at the corners indicate the ϕ10 bolts used for the measurement target. However, in the results of Series A, cracks occurred near these bolts; thus, for Series B the measurement targets were attached by adhesive.

Shear cracks occur at the centers of the walls. In S110 and M50, where the rebar spacing is small, diagonal cracks gradually formed toward the corners of the wall after the crack was generated at the center. Finally, the total number of consecutive diagonal cracks, which is the sum of the positive and negative sides during the ultimate deformation

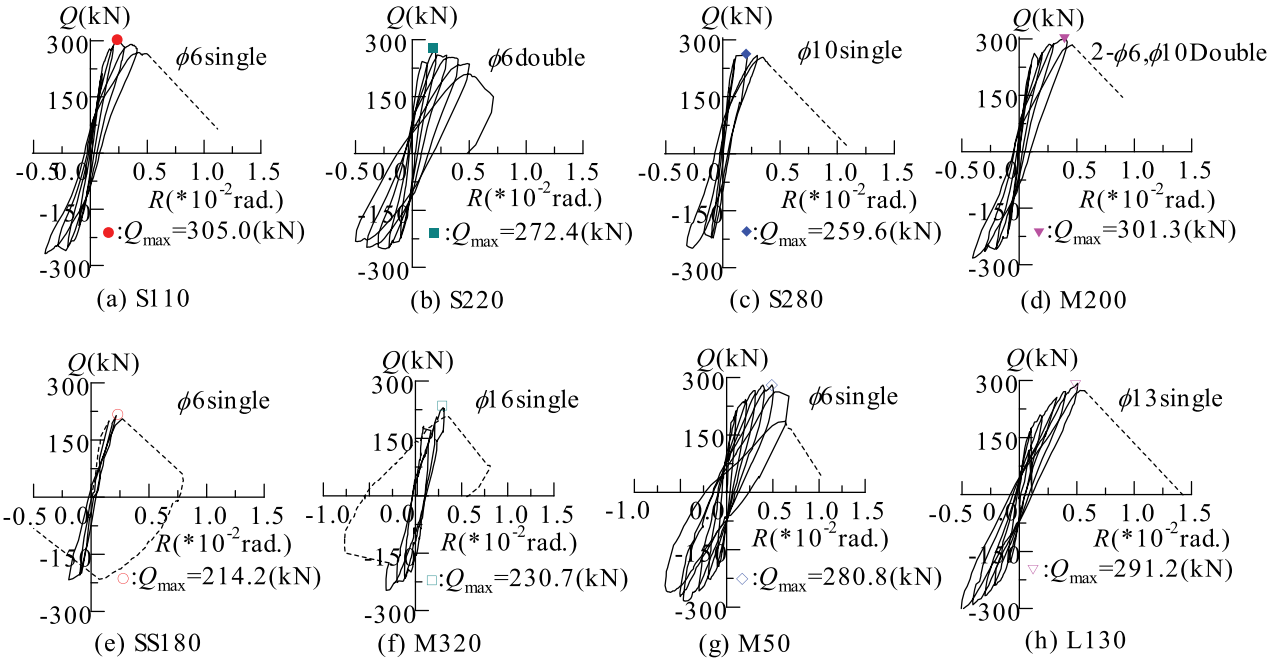

Figure 6. Load deformation curve.

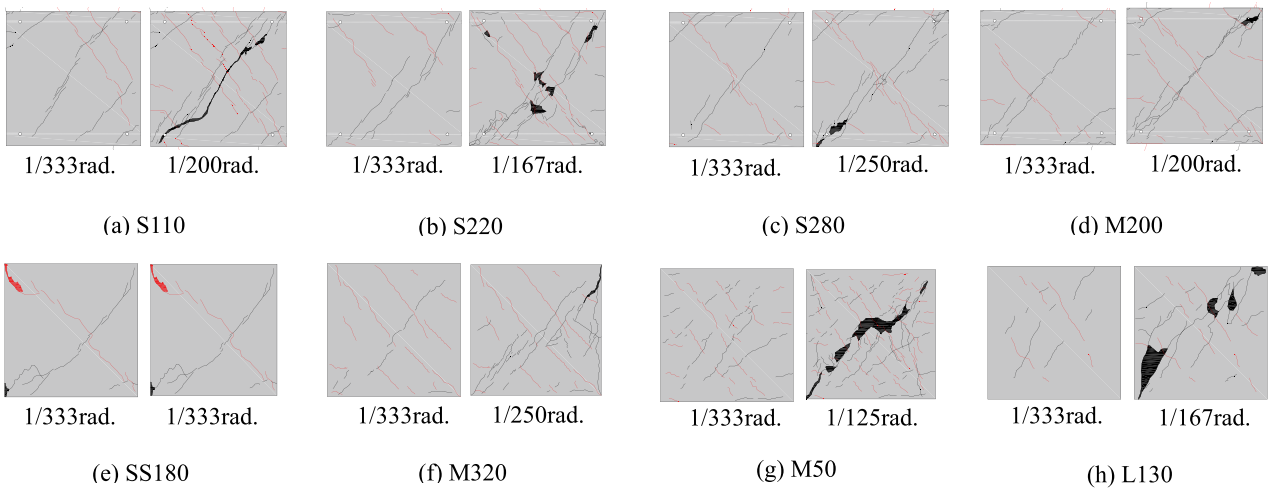

Figure 7. Crack patterns: the figures on the right indicate crack patterns at the point of ultimate deformation.

(as shown in Figure 7), was approximately ten in these two specimens.

However, in S280, where the rebar spacing is the second widest amongst all, the total number of diagonal cracks was about four. Furthermore, in SS180, where p_w is the smallest amongst all, there were only two diagonal cracks. This indicates that the number of cracks reduces with a wider rebar spacing, or by reducing p_w.

2.4.3. Crack width

Figures 8 and 9 show the maximum crack width ω behavior up to the maximum load and the maximum residual crack width behavior, respectively. In these figures, **(a)** and **(b)** differ only in the range of the axis scales.

Focusing on specimens with the same p_w in Figure 8 (b), the crack widths widen as the rebar spacing increases. The same tendency is also observed in Figure 9. In Section 4, the maximum crack widths are estimated using the proposed method.

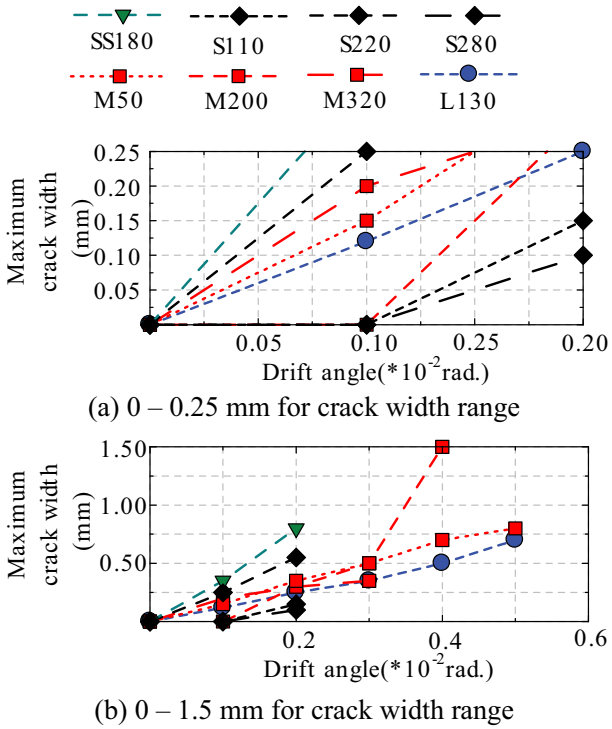

Figure 8. Maximum crack width transition: (a) and (b) utilize different scales on the x and y axes.

3. Finite element analysis

3.1. Outline of analysis

Although the shear-strength formula (e.g. Equations (1a) and (1b)) does not consider the rebar spacing, the test results confirmed that the rebar spacing affected the maximum shear loads. The stress field of the nonstructural wall subjected to shear load is investigated to determine the reason. To qualitatively evaluate a stress distribution, finite-element (FE) analysis is conducted. For this purpose, S110, S220, and S280 are modeled. In this study, 2D finite-element (FE) analysis is conducted by using DIANA 10.3, which is a general software (DIANA FEA BV 2019). In addition, the accuracy would be higher because of tuning many analytical conditions with complex, while a complex modelling might not be applied to other specimens. Thus, since the purpose of this analysis is to qualitatively evaluate the stress distribution, constitutive laws are modeled as simple as possible.

Furthermore, a smeared crack model is typically used for non-linear FE analyses of RC structures. However, it is not possible to quantitatively evaluate the crack position. It is thought that rebar spacing is a very important factor affecting the crack pattern. Therefore, a discrete crack model (e. g. Lu, Ridha, and Tay 2019) is also applied in this study. In previous papers, this model has been applied to beam analysis (Pham et al. 2019), masonry analysis (Urrego et al. 2018) and others. When the discrete crack model is used, the crack positions can be determined before calculation. This model is applied to

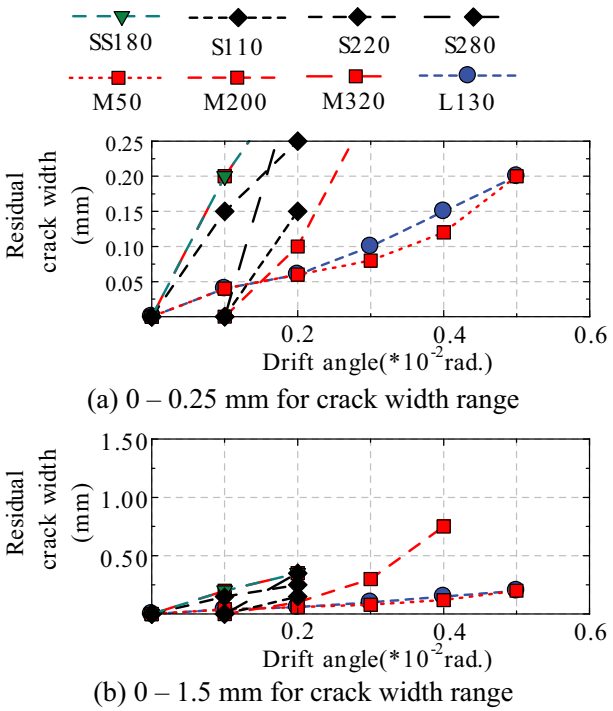

Figure 9. Residual crack width behavior: (a) and (b) utilize different scales on the x and y axes.

a nonstructural wall and compared it with the smeared crack model.

3.2. Finite element analysis model

Figure 10 shows the FE analysis model. In the figure, the model for S110 is illustrated as an example. The mesh is divided into squares of approximately 40 mm. A plane stress element and an embedded rebar element are applied to the concrete and rebar.

In the loading tests, antisymmetric shear loading was applied; therefore, the upper loading beam was left free in the *x* direction, and the nodes of both its edges were restrained so that both *y* displacements had the same value. The nodes of the bottom loading beam were fixed in both displacement and rotation.

3.3. Discrete model

Figure 11 shows the geometric configurations of the walls. The shear strength increased and the crack width decreased as the rebar spacing decreased. To introduce a discrete crack model into a wall, the crack positions need to be determined. Although the positions can be figured out by test specimens, an experimental test is also essential. Thus, this technique is not useful. Therefore, in this research, the number of cracks and their positions are calculated using the crack interval s_{av}. (Matsubayashi et al. 2018)

$$s_{av} = 2\left[c + \frac{2s}{10}\right] + k_1 k_2 \frac{\phi}{p_w} \quad (3)$$

Here, k_1 = 0.4. k_2 = 0.25 when $s \leq 15\phi$, and 0.1 when $s > 15\phi$. The number of cracks can be calculated by dividing the wall diagonal length by s_{av}.

Table 6 shows the crack intervals by Equation (3) and the tests. However, differences between s_{av} and s_{exp} are big in M200 and SS180, while s_{av} is roughly a good match with s_{exp} for the other specimens. Therefore, it can be judged that Equation (3) is useful for estimating the crack interval of nonstructural walls.

In addition, spring elements are applied to the intersections of discrete cracks and rebars.

3.4. Material properties

3.4.1. Concrete

The constitutive law of concrete is shown in Figure 12. The constitutive law on the tensile side is different between the wall and loading beam. In the wall of the discrete crack model, the elasticity model is applied to the stress–strain curve because the tensile behavior can be evaluated by the discrete crack model. In both the upper and lower loading beams, the wall of the smeared crack model, the Izumo model (Tamai et al. 1987) is applied. The Izumo model accounts for tension

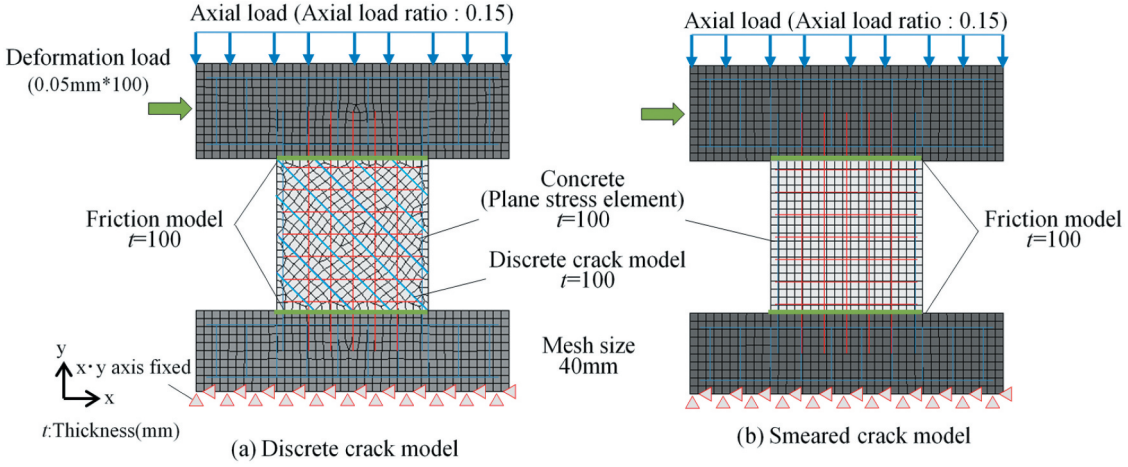

Figure 10. Finite element analysis model.

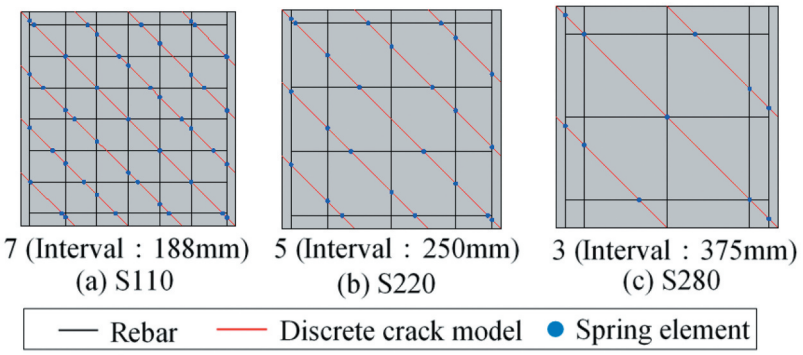

Figure 11. Geometric configurations.

Table 6. Crack interval by Eq.(3) and tests.

Specimens	S110	S220	S280	M200	SS180	M320	M50	L130
s_{av} (mm)	199	265	352	202	265	291	175	240
N	5	3	2	3	1	2.5	5.5	4
s_{exp} (mm)	177	265	354	265	495	283	152	198

N: The average number of consecutive diagonal cracks on positive and negative side at ultimate deformation.
s_{exp}: The crack spacing of the test = $l0/(N+1)$.

stiffening, which is caused by a stress redistribution of a bond stress after cracking. As mentioned above, in this analysis, tension stiffening is taken into account instead of applying a bond stress – slip relation between concrete and rebar, and a tensile fracture energy of concrete.

The Izumo model is described by the following equation:

$$\sigma = \begin{cases} E_c \bar{\varepsilon} for\, 0 < \bar{\varepsilon} < \varepsilon_e \\ f_t \times \left(\frac{\varepsilon_{tu}}{\bar{\varepsilon}}\right)^c for \bar{\varepsilon} \geq \varepsilon_e \end{cases} \tag{4}$$

Constitutive laws on the compressive side are common for both the wall and the loading beams. In the stress-strain curve, the Thorenfeldt model (e.g. DIANA FEA BV 2019; Choi et al. 2014) is applied and described by Equations (5) – (8).

$$f = \left[\frac{n\left(\varepsilon_c/\varepsilon_p\right)}{n-1+\left(\varepsilon_c/\varepsilon_p\right)^{nk}}\right] f_c \tag{5}$$

$$n = 0.8 + \frac{f_c}{17} \tag{6}$$

$$k = \begin{cases} 1 & |\varepsilon_p < \varepsilon_c < 0 \\ 0.67 + \frac{f_c}{62} & |\varepsilon_c \leq \varepsilon_\pi \end{cases} \tag{7}$$

$$\varepsilon_p = \frac{n}{n-1} \cdot \frac{f_c}{1000 E_c} \tag{8}$$

Additionally, from the test results, a significant compressive failure of concrete was not observed. Therefore, the compressive fracture energy, as well as the tensile fracture energy was not taken into account.

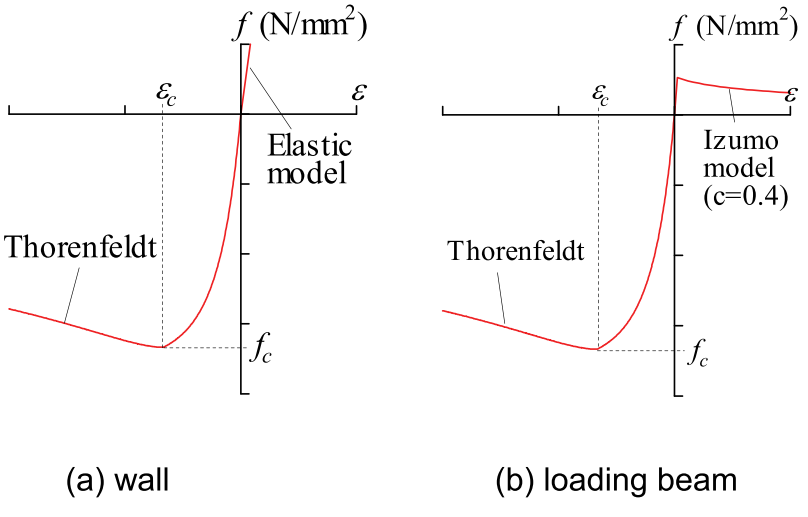

Figure 12. Concrete constitutive law.

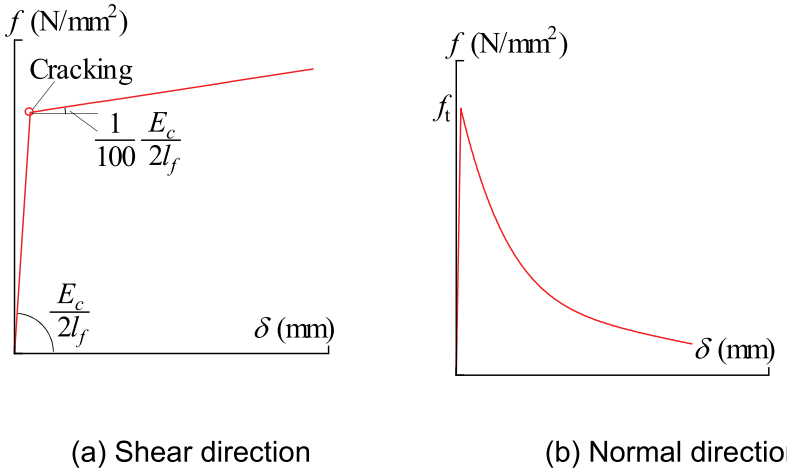

Figure 13. Discrete crack model constitutive law.

3.4.2. Rebar

The bilinear model based on von Mises yield criterion is used for the constitutive law of the rebar. The free length of the spring element l_f is 20 mm, considering the maximum aggregate size.

3.4.3. Discrete crack model

The constitutive laws of the discrete crack model are shown in Figure 13. A bi-linear model is applied in the shear direction. The shear stiffness can be calculated from E_c and the free length l_f when the Poisson's ratio λ is 0. After cracking, this stiffness reduces to $^1/_{100}$ of the initial stiffness.

In the normal direction, the stiffness is calculated from E_c for l_f. The Hordijk model (Hordijk 1992) is applied to evaluate stress softening after cracking. This model is described by Equation (9):

$$\frac{\sigma}{f_t} = \left(1 + \left(3\frac{w}{w_c}\right)^3\right) exp\left(-6.93\frac{w}{w_c}\right) - \frac{w}{w_c}(1 + 3_3) exp(-6.93) \quad (9)$$

where $w_c = 5.136\, G_f/f_t$.

Hence, it is thought that the analysis result is affected by dilatancy. However, the purpose of this analysis is to perceive stress distribution. Therefore, in this analysis, the shear and normal behavior are separated without considering the effect of dilatancy.

3.4.4. Friction model between wall and loading beams

The friction model is used between the wall and the loading beam to evaluate the cracking behavior at these boundaries. The constitutive laws are illustrated in Figure 14. With this model, the friction of the concrete and the dowel action of the rebar are taken into account. Because the wall and the loading beam are rigidly joined, the friction coefficient is set to 1.4 based on the AIJ guidelines (AIJ 2002). Therefore, the frictional force is obtained by multiplying this coefficient by the axial force. After the friction force reaches a maximum it remains constant. The shear load resulting from the dowel action is also added to the friction. The shear resistance of the rebar is calculated based on a previous study (Takase 2019). An elastic model is applied in the normal direction on the compressive side, while a perfect elasto-plastic model is applied on the tensile side. In Figure 14(b), f_n is the average stress of both the total yield strength of the rebar and the tensile strength of the concrete.

3.5. Loading conditions

Monotonic forced shear displacement is applied to the model with a 0.05 mm pitch. The maximum number of iterations is 50. The Newton–Raphson method is applied to a convergence calculation.

3.6. Analysis results

Figure 15 shows the analytical results of the load – deformation (Q – R curves). The black line indicates the test results. The red and blue lines show the analytical results of the discrete crack model and the smeared crack model, respectively. The maximum

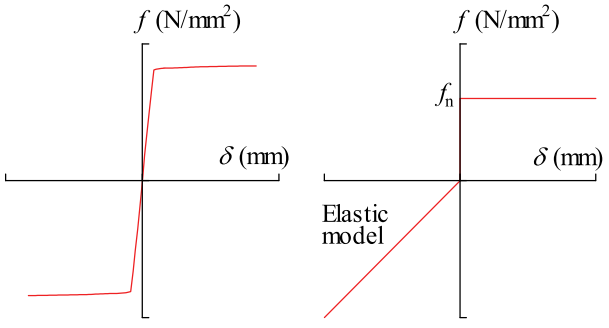

Figure 14. Friction model constitutive laws.

shear load Q_{max} and the deformation angle at peak R_{max} are listed in Table 7.

Figure 15 shows that the analytical results of the discrete crack model roughly match the test results. However, the results of the smeared crack model are not aligned with the test results. From Table 7, it can be seen that the R_{max} values of the smeared crack model are larger than those of the tests.

Hence, the results of the smeared crack model are focused upon. When diagonal cracks were observed at the center of the wall, the stiffness of the $Q - R$ curves reduced. Hereafter, the strains of the horizontal wall rebar, which are arranged in the center, increased and the rebar yielded. Therefore, the shear load became approximate constant. In addition, in this paper, although the discrete crack models were used without considering dilatancy, it was possible to roughly estimate the skeleton curves of the tests.

Figure 16 shows the distribution of the maximum principal stress at approximately R_{max}. Figure 16(a), which presents the results of the discrete crack model, illustrates how the stress distribution differs depending on the rebar spacing. On the other hand, according to the results of the smeared crack model, the differences in rebar spacing are small. As mentioned above, to investigate the effect of the rebar spacing, the discrete crack model is more suitable than the smeared crack model.

Observing Figure 16 again, the stress is distributed evenly over the entire S110 specimen. However, the stress distribution is uneven in S280. Therefore, it is thought that the stress cannot be distributed on the entire wall with wider rebar spacing, and Q_{max} then becomes small.

4. Proposal of crack width calculation formula

As mentioned in the preceding chapters, the shear strength decreased as the damage increased. Furthermore, the discrete crack model is useful for nonstructural walls, or for evaluating rebar spacing. As described before, to analyze this model, the crack position or crack spacing are needed. For these results, a method to evaluate the cracking behavior is useful for structural performance design or repair cost estimation after earthquakes. A prediction method is proposed using the previous equation for crack width; this section details the proposed method.

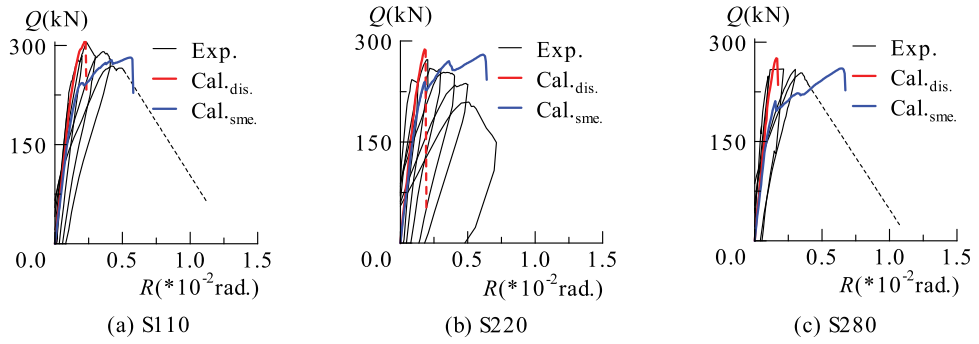

Figure 15. Analysis result (load deformation curve).

Table 7. Maximum shear load of analysis and tests.

	S110			S220			S280		
	Exp.	Cal.$_{dis.}$	Cal.$_{sme}$	Exp.	Cal.$_{dis.}$	Cal.$_{sme}$	Exp.	Cal.$_{dis.}$	Cal.$_{sme.}$
$Q_{max.}$(kN)	305.0	312.2	281.7	272.4	287.8	256.3	259.6	277.5	260.4
$R_{max.}$ (*10^{-2} rad)	0.23	0.23	0.55	0.20	0.18	0.31	0.21	0.16	0.64

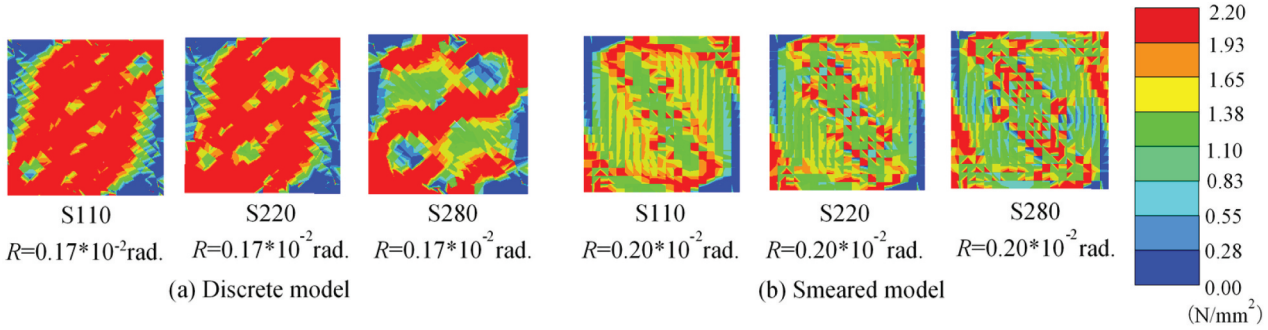

Figure 16. Distribution of the maximum principal strain.

A formula to estimate the average shear crack width of an I-shaped pre-stressed reinforced concrete beam was proposed (Silva, Mutsuyoshi, and Witchukreangkrai 2008). Based on this formula, the following equation was proposed: (Matsubayashi et al. 2018).

$$w_{max} = k_w s_{av} \varepsilon_{max} cos\theta \tag{10}$$

where, k_w = 1.2. (Silva, Mutsuyoshi, and Witchukreangkrai 2008; Matsubayashi et al. 2018)

In short, w_{max} can be obtained by multiplying the crack spacing by the strain. Hence, k_w is an experimental coefficient, and cos θ is multiplied to convert a horizontal rebar strain into a strain in the direction of the crack spacing.

In a previous study, ε_{max} was obtained by FE analysis (Matsubayashi et al. 2018). However, it is too difficult to conduct an FE analysis for every trial. Therefore, in this study, a simple method is proposed to calculate ε_{max} from the geometrical deformation. Figure 17 shows an image of the proposed method; the dotted and solid lines indicate the wall shape before and after loading, respectively.

When a horizontal forced displacement is applied, the wall also deforms vertically. However, it is difficult to evaluate this vertical displacement. For this reason, in this study, the diagonal strain γ_{max} is calculated using only horizontal displacement with the following formula:

$$\gamma_{max} = \frac{x \cdot \sin\theta}{l_0} \tag{11}$$

Here, it is assumed that the rebar strain corresponds with γ_{max} because the deformation is sufficiently small compared to the wall size. ε_{max} is calculated by multiplying γ_{max} by k_{max}.

$$\varepsilon_{max} = k_{max} \cdot \gamma_{max} \tag{12}$$

Hence, γ_{max} is an average strain; however, a local strain is required to evaluate the maximum strain. Therefore, k_{max}, which is the coefficient to convert an average strain to a local strain, is multiplied by γ_{max} .

From the analysis results, k_{max} is calculated with using a coefficient of variation, which is a value obtained by dividing the standard deviation by an average value, of all rebar strain values from S110, S220, and S280 during R_{max}. Because the average coefficient of variation was approximately equal to 0.7, the value of k_{max} was set to 1.7, so as to add the variation to the average strain.

Figure 18 shows a comparison of the calculated crack width with the test results. The calculated crack width is the value at the peak load of each loading cycle. Therefore, the x axis intend a normal drift angle. Additionally, the residual crack widths were also measured in this tests. A prediction method of a residual crack width or a residual drift angle will also be focused upon in future work.

The calculated crack widths are in rough agreement with the test results for all specimens. However, it is difficult to evaluate the test results when the crack width is 0 mm or the width widens rapidly. Moreover, although the test results show curved behaviors, the calculated results are linear. For this reason, the equation of the strain is linear to the shear deformation. As only square-shaped walls were tested in this study, it will also be necessary to investigate specimens with different shear-span ratios in the future. Nevertheless, it is thought that the proposed equations will be useful for crack width prediction in the engineering field.

5. Conclusion

In this study, the structural properties of nonstructural walls were investigated. The findings of this research are as follows:

(1) The crack width increased as the rebar spacing increased or the rebar ratio decreased. Thus, the damage quantity was affected by the rebar spacing and ratio.
(2) The shear strength decreased as the rebar spacing increased. Therefore, it can be understood that the damage quantity increases as the shear strength decreases. The lower limit of the shear strength could be estimated by ${}_{su}Q_{min}$ except for M320, of which the rebar spacing exceeds 300 mm.

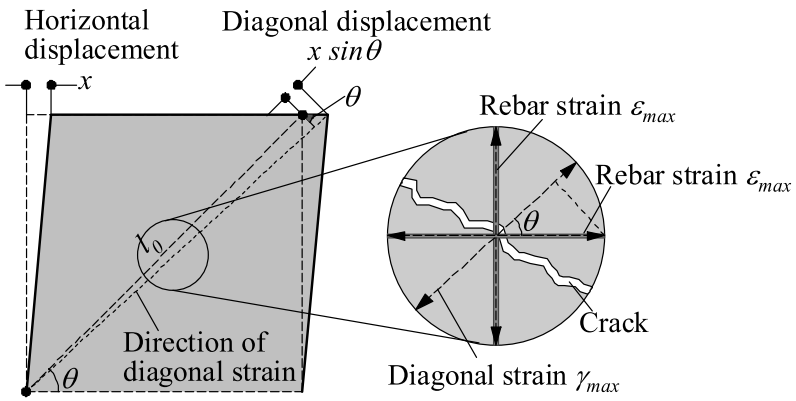

Figure 17. Image of strain.

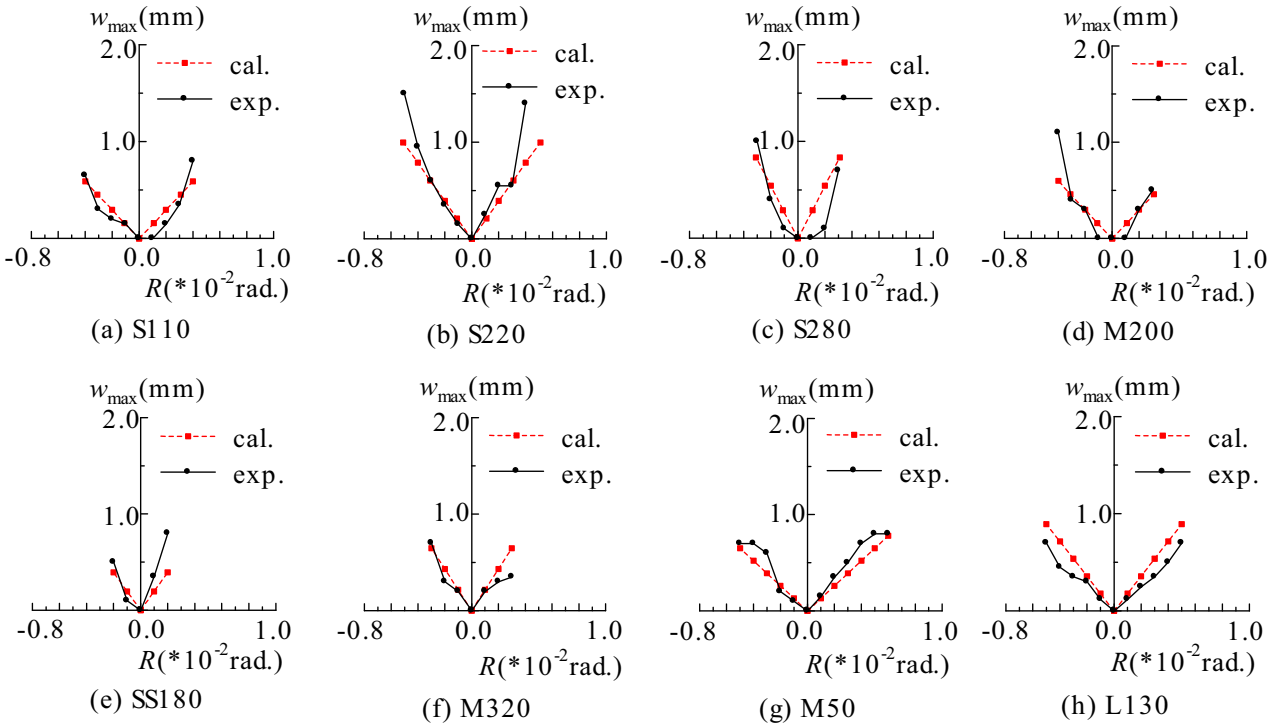

Figure 18. Comparisons of crack width.

(3) To evaluate a stress distribution, two basic types of FE analyses were conducted. The results of the smeared crack model did not match well with the skeleton curves of S110, S220, and S280. In other words, the difference in the rebar spacing cannot be properly accounted for by the smeared crack model. However, by using the discrete crack model, the test results could be well predicted until the peak load.

(4) According to the results of the FE analysis of the discrete crack model, the stress field was more localized with wider rebar spacing. Therefore, it was concluded that the shear strength decreased as the rebar spacing increased.

(5) The prediction method of the shear crack width and a simple formula for estimating rebar strain from geometrical deformation were proposed. Furthermore, in this method, a coefficient k_{max}, which was calculated by using the variation of the analytical rebar strains, was introduced to estimate a local rebar strain. The cracking behavior could be reasonably predicted using the proposed method.

In future work, a shear strength formula considering rebar spacing will be formulated, and a structural design method will also be created, taking crack behavior into consideration. Although, some issues some still remain, it is our hope that these findings will be useful for evaluating the performance design of non-structural walls.

List of Nomenclatures

a_0	the section area of a pair of the wall rebar
a_t	the section area of the opening reinforcement bars
a_{se}	the section area of the wall rebar
b	the equivalent wall thickness
c of Eq.(3)	the cover concrete
c of Eq.(4)	the exponent coefficient for the anchorage of a rebar (c = 0.4 for this test)
f_c	the concrete compressive strength
f_t	the concrete split strength
f_{wy}	the yield strength of the wall reinforcement bar
f_y	the yield strength of the opening reinforcement bar
h	the height of the wall
h_w	the height of the inflexion point (= h/2 for this test)
j	the stress center distance
l	the length of the wall
l_0	the diagonal length of the wall
l_t	the length between the opening reinforcement bars (≅ l_w)
l_w	the effective wall length (= 0.8 l for a wall without columns (AIJ 2010)
p_{se}	the wall rebar ratio (= $a_0/(b$ x $s)$)
p_t	the tensile rebar ratio (opening rebar and wall cross section ratio)
s	the rebar spacing
w	the crack width
w_c	the critical crack width
x	the horizontal displacement
G_f	the fracture energy
M/Qd	the shear span ratio (= 0.5 in this tests)
$\bar{\varepsilon}$	the average strain
ε_c	the concrete strain

ε_e	the strain at maximum tensile stress
ε_{max}	the maximum strain of the rebar at each deformation angle
ε_p	the concrete strain at the maximum compressive stress
ε_{tu}	the crack generation strain
ϕ	the rebar diameter
θ	the diagonal angle
σ	the average stress
σ_0	the compressive axial stress (= 0.15 x f_c in this test)

Disclosure statement

No potential conflict of interest was reported by the authors.

References

Architectural Institute of Japan (AIJ). 2002. *AIJ Guidelines for Structural Design of Precast Concrete Connection Emulating Cast-in-Place Reinforced Concrete*, 60–61. Japan. (in Japanese).

Architectural Institute of Japan (AIJ). 2010. *AIJ Standard for Structural Calculation of Reinforced Concrete Structures*, 292–293, 8th ed. Japan. (in Japanese).

Choi, J. H., K. H. Jung, T. K. Kim, and J. H. J. Kim. 2014. "Analytical and Experimental Studies on Torsional Behavior of Hybrid Truss Bridge Girders with Various Connection Joints." *Journal of Advanced Concrete Technology* 12 (11): 478–495. doi:10.3151/jact.12.478.

DIANA FEA BV. 2019 "User's manual-Release 10.3." https://dianafea.com/manuals/d103/Diana.html

Fukui, S., Y. Sanada, and R. Yoon. 2019. "Analytical Study on Axial Compression on RC Secondary Flat Walls under Seismic Loads." *Journal* of *Structural* and *Construction Engineering, AIJ* 84 (765): 1465–1474. (in Japanese). doi10.3130/aijs.84.1465.

Hordijk, D. A. 1992. "Tensile and Tensile Fatigue Behavior of Concrete; Experiments, Modelling and Analyses." *HERON* 37 (1): 3–79.

Japan Building Disaster Prevention Association (JBDP). 2017. *Evaluation and Retrofit Guideline for Reinforced Concrete Building (Revision 2001)*. (in Japanese).

Lu, X., M. Ridha, and T. E. Tay. 2019. "Adaptive Discrete-smeared Crack (A-disc) Model for Multi-scale Progressive Damage in Composites." *Composites Part A* 125: 105513. doi:10.1016/j.compositesa.2019.105513.

Maidiawati, Sanada, Y., D. Konishi, and J. Tanjung. 2011. "Seismic Performance of Nonstructural Brick Walls Used in Indonesian R/C Building." *Journal of Asian Architecture and Building Engineering* 10 (1): 203–210. doi:10.3130/jaabe.10.203.

Matsubayashi, M., Y. Takase, M. Mizoguchi, and K. Inoue. 2018. "Estimation of Crack Width of Non-structural Walls Using Finite-element Analysis." *Journal of Advanced Civil Engineering Practice and Research* 6: 18–25.

Pham, D. C., X. Cui, X. Ren, and J. Lua. 2019. "A Discrete Crack Informed 3D Continuum Damage Model and Its Application for Delamination Migration in Composite Laminates." *Composites, Part B* 165: 554–562. doi:10.1016/j.compositesb.2019.02.045.

Sanada, Y., R. Yoon, T. Akahori, Y. Ojio, H. Choi, and Y. Kim. 2017. "Softening Effects of RC Nonstructural Flat Walls on Ductile Concrete Building." *Earthquake Engineering Structural Dynamics* 46 (10): 1645–1665. doi:10.1002/eqe.2874.

Silva, D. S., H. Mutsuyoshi, and E. Witchukreangkrai. 2008. "Evaluation of Shear Crack Width in I-Shaped Reinforced Concrete Beams." *Journal of Advanced Concrete Technology* 6 (3): 443–458. doi:10.3151/jact.6.443.

Sousa, L., and R. Monteiro. 2018. ""Seismic Retrofit Options for Non-structural Building Partition Walls." *Impact on Loss Estimation and Cost-benefit Analysis." Engineering Structures* 161: 8–27. doi:10.1016/j.engstruct.2018.01.028.

Suzuki, T., Y. Sanada, and H. Choi. 2017. "Field Investigation and Seismic Performance Evaluation by Nonlinear Analysis of an R/C Building with Secondary Walls Damaged by the 2016 Kumamoto Earthquake." *Journal Struct. Constract. Engineering, AIJ* 82 (740): 1663–1673. (in Japanese). doi10.3130/aijs.82.1663.

Takase, Y. 2019. "Testing and Modeling of Dowel Action for a Post-installed Anchor Subjected to Combined Shear Force and Tensile Force." *Engineering Structures* 195: 551–558. doi:10.1016/j.engstruct.2019.05.086.

Takase, Y., T. Ikeda, and T. Suzumura. 2015 "Seismic Retrofitting Effect of 10-story Residential Building Retrofitted Using Passive Seismic Control System with Amplifier Mechanism." 5th International Conference on Computational Methods in Structural Dynamics and Earthquake Engineering, pp. 3934-3945. Crete Island, Greece. doi:10.7712/120115.3669.1161

Tamai, S., H. Shima, J. Izumo, and H. Okamura. 1987. "Average Stress-average Strain Relationship of Steel in Uniaxial Tension Member in Post-yield Range." *JSCE* 378 (6): 239–247. (in Japanese).

Tani, M., E. Yuniarsyah, T. Mukai, and S. Kono. 2015. "Experimental Test for Damage Reducing and Improvement of Structural Performance of R/C Non-structural Walls." *Proceedings of JCI* 37 (2): 901–906. (in Japanese).

Tsai, M. H., and T. C. Huang. 2011. "Progressive Collapse Analysis of an RC Building with Exterior Non-Structural Walls." *Procedia Engineering* 14: 377–384. doi:10.1016/j.proeng.2011.07.047.

Urrego, L. B., E. Verstrynge, G. Giardina, and K. V. Balen. 2018. "Crack Growth in Masonry: Numerical Analysis and Sensitivity Study for Discrete and Smeared Crack Modelling." *Engineering Structures* 165: 471–485. doi:10.1016/j.engstruct.2018.03.030.

Yoon, R., Y. Sanada, and T. Akahori. 2017. "Seismic Performance Evaluation of RC Moment-Resisting Frames with Typical Non-Structural Walls in Japan." *Journal of Advanced Concrete Technology* 15 (9): 544–557. doi:10.3151/jact.15.544.